Preprint Cambridge Centre for Computational Chemical Engineering ISSN 1473 – 4273

The impact of cyclic fuels on the formation and structure of soot

Maurin Salamanca[1,2], Maria Botero[3], Jacob W. Martin[1,2], Jochen A. H. Dreyer[1,2,4], Jethro Akroyd[1,2], Markus Kraft[1,2,5]

released: November 27, 2019

[1] Department of Chemical Engineering
and Biotechnology
University of Cambridge
Philippa Fawcett Drive
Cambridge, CB3 0AS
United Kingdom

e-mail: mk306@cam.ac.uk

[2] CARES
Cambridge Centre for Advanced
Research and Education in Singapore
1 Create Way
CREATE Tower, #05-05
Singapore, 138602

[3] Departamento de Ingeniería Mecánica
Universidad de Antioquia
Medellín
Colombia

[4] CoaST Department of Chemical and
Biochemical Engineering
Technical University of Denmark (DTU)
Building 229
Kgs.Lyngby 2800
Denmark

[5] School of Chemical
and Biomedical Engineering
Nanyang Technological University
62 Nanyang Drive
Singapore, 637459

Preprint No. 246

UNIVERSITY OF CAMBRIDGE

Keywords: Soot formation, coflow diffusion flames, five-membered rings, pentagonal rings, particle size distribution, polycyclic aromatic hydrocarbons

Edited by
Computational Modelling Group
Department of Chemical Engineering and Biotechnology
University of Cambridge
Philippa Fawcett Drive
Cambridge CB3 0AS
United Kingdom

E-Mail: c4e@cam.ac.uk
World Wide Web: http://como.ceb.cam.ac.uk/

Abstract

This paper investigates the impact of cyclic fuels on the nanostructure, nucleation and overall production of soot in an *n*-heptane (C_7H_{16}) laminar coflow diffusion flame. The fuels selected to dope the *n*-heptane flames are cyclopentene (C_5H_8), cyclohexene (C_6H_{10}) and methylcyclohexane (C_7H_{14}). These fuels were chosen for their differences in their structure and sooting tendency. The flame structure was studied with Differential Mobility Spectrometry (DMS) for particle size distribution determination, two-colour ratio pyrometry to calculate the soot volume fraction and soot temperature. The soot nanostructure was investigated using Raman spectroscopy and high-resolution transmission electron microscopy (HRTEM). The addition of cyclic fuels was found to promote the formation of soot nanoparticles earlier in flames. In addition, the soot volume fraction was increased significantly by the addition of the cyclic fuels, especially by the addition of cyclopentene. The addition of 20% of cyclopentene increased the soot volume fraction by a factor of 2. HRTEM results suggest a significant influence of cyclopentene on the soot nanostructure; cyclopentene addition promotes the incorporation of five-membered rings (pentagonal rings) leading to highly curved fringes. This suggests cyclopentene could be used as a fuel to promote curvature in different carbonaceous structures to modify their properties.

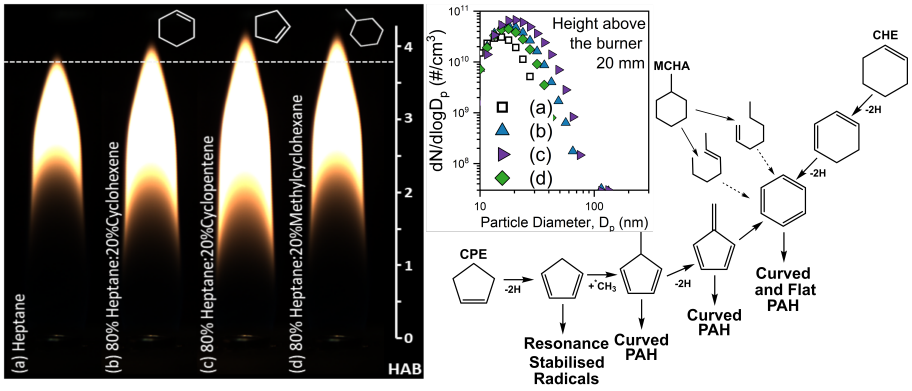

Highlights

- Cyclic fuels promote soot formation in aliphatic flames.
- The soot nanostructure changes with the addition of cyclopentene.
- Cyclopentene promotes the formation of highly curved fringes and curvature integration.

Contents

1 Introduction

Particulate matter emissions from incomplete combustion of hydrocarbons contribute to climate change [6, 44] and have adverse effects on human health [3, 49]. Even with significant efforts to reduce pollutant emissions into the atmosphere, the combustion of fossil fuels for ground, maritime and air transport remains the most important source of particulate matter emissions [68]. The formation of such particulate matter, also know as soot, has been widely studied in the last decades; however, the transition between the gas phase and nanoparticles, called nucleation, is still not well understood [87]. The understanding of the nucleation of carbonaceous nanoparticles (CNP) is essential to improve the strategies to minimise particulate matter emissions.

Particulate formation has been studied in a variety of different laminar flame configurations [14, 43, 67, 87]. Laminar flames are of particular interest for studying soot formation. In coflow diffusion flames, soot particles are generated near the high-temperature regions of the flame reaction zone (fuel-side annulus) and are transported up the flame and towards the centreline through convection and possibly by thermophoresis [27]. Recently, methane and ethene coflow diffusion flames were selected by the International Sooting Flame Workshop (ISF) [69] and have been studied by techniques such as colour-ratio pyrometry, time-resolved Laser-Induced Fluorescence (LIF) and Laser-Induced Incandescence (LII) [5, 42, 62]. The combination of these techniques allowed the transition between aromatic-based nanostructures to soot to be observed. According to Bartos et al. [5], high concentrations of nanoparticles are found to precede the higher soot volume fraction (f_v) found in fuel-rich sooty flames, although not proportionally, suggesting that surface growth strongly contributes to f_v in the high sooting flames. In the high sooting flames, the majority of particle formation shifts from the centreline to the wings at the outer edges of the flame closer to stoichiometric conditions [81]. Particle formation in the wings of the flames occurs in the presence of oxygen and higher temperatures, resulting in particles with spectroscopic properties resembling those formed towards the oxidiser side of counter-flow diffusion flames [5, 27]. These flames have also allowed for the characterisation of the sooting tendency of different fuels [15], the effect of temperature and pressure in soot formation [1, 28, 52], and the soot particles composition [20, 38, 66], and thus further insights into such flames offer a large body of research for comparison.

Polycyclic aromatic hydrocarbons (PAH) have been recognised as precursors for soot formation [14, 67, 87], including five-membered rings (pentagonal rings) [35, 46, 75]. The incorporation of pentagonal rings contributes to the formation of small curved polycyclic aromatic hydrocarbons (cPAH). Experimental evidence of five-membered rings has been found in aliphatic [37, 39, 70] and aromatic flames [47]. Five-membered rings can be formed by the bimolecular reactions of C3 (allyl or propargyl radicals) and C2 (ethene or ethyne) species [24, 64]; or by the partial oxidation of benzene through a phenoxy radical and unimolecular elimination of CO [36, 58]. Moreover, recent high-resolution transmission electron microscopy (HRTEM) studies have shown that a significant fraction of cPAH is present in soot [8, 54, 86]. The curvature analysis of the fringes indicates the integration of one to three embedded pentagonal rings in the cPAH molecules [2, 8, 54].

This evidence supports the idea that a significant proportion of five-membered rings are present in incipient carbon nanoparticles [53, 54]. The electronic structure calculations

of cPAH revealed the presence of a permanent dipole moment due to the flexoelectric effect [53]. Furthermore, the dimerisation energy of cPAHs with one or two pentagonal rings were found to be comparable to that of similar-sized planar PAHs [54]. These curved structures are stable at flame temperature [56]. Moreover, it has been demonstrated that the reaction leading to the conversion of a planar PAH to a curved one through ring addition at an armchair site is very fast at temperatures below 2000 K [73]. These results suggest a significant role of the five-membered rings in the formation of incipient carbon nanoparticles. Whether the five-membered rings are directly incorporated or formed in the edges of larger PAHs in the growth process is not yet determined. There is a lack of experimental evidence to correlate the fuel structure and the incorporation of five-membered rings in soot nanoparticles.

The purpose of this paper is to gain new insights into the sooting propensity of cyclic fuels relative to linear alkanes and to understand the influence of the fuel structure on the incorporation of five-membered rings (pentagonal rings) and the changes induced on the soot nanostructure. For this reason, we have chosen laminar coflow diffusion flames at atmospheric pressure and investigated blends of *n*-heptane and three cyclic fuels, namely cyclohexene (C_6H_{10}), cyclopentene (C_5H_8) and methyl cyclohexene (C_7H_{14}). *n*-heptane was selected as the base flame because it is a good surrogate for gasoline and diesel. Cyclohexene, cyclopentene and methylcyclohexane were selected due to their structural differences in ring size and methyl substitution.

2 Experimental methodology

The experimental set-up has been reported previously [18]. In brief, four atmospheric pressure, non-premixed, laminar *n*-heptane/cyclic fuel/air flames were stabilised on a Yale coflow steady flame burner [26]. In all of the experiments, the total carbon flow rate from the two components in the binary mixtures was kept constant with respect to the *n*-heptane to facilitate comparison among the fuels. The fuels (*n*-heptane/cyclic fuels) were mixed as liquids to obtain a 20% carbon mol substitution of the pure *n*-heptane flame. The mixture of liquid fuels was injected into a CEM evaporator (Bronkhorst), at 323 K, using a syringe pump. In the evaporator, the liquid fuel blend was mixed with 200 mL min^{-1} of Argon (99.99%). The fuel/carrier gas mixture was transferred to the burner using tubes heated via temperature-controlled heating tapes at 423 K. In all cases, compressed air (50 L min^{-1}) was used for the coflow.

The fuels that were selected to dope the *n*-heptane flame were cyclopentene, cyclohexene, and methylcyclohexane. The fuels structure and notation used to identify the flames are summarised in Table 1. *n*-heptane (99.8%) was supplied by VWR, cyclopentene (>98.0%), cyclohexene (>99.0%) and methylcyclohexane (>99.0%) were supplied by Tokyo Chemical Industry (TCI). All the fuels were liquid at room temperature, with liquid-phase flow rates ranging from 6.98 to 7 g h^{-1} depending on the liquid mixtures mass density, which were measured as part of this work.

Table 1: *Flame notation, cyclic fuel structure and visible flame length.*

Flames	Notation	Structure	Length (mm)
n-heptane	HEP	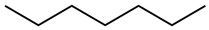	37.0
80% *n*-heptane: 20% cyclohexene	HEP:20CHE		39.0
80% *n*-heptane: 20% cyclopentene	HEP:20CPE	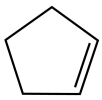	40.5
80% *n*-heptane: 20% methylcyclohexane	HEP:20MCHA	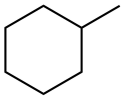	40.3

2.1 Flame temperature

Centreline temperature measurements were performed with an uncoated 125 μm R-type thermocouple, using a rapid insertion procedure [61]. The details for the set-up used in the temperature measurements, as well as the correction due to radiative heat losses from the thermocouple bead, are described in full by Dreyer et al. [18].

2.2 Particle size distribution

In this study, a sampling probe based on the design reported by Hepp and Siegmann [33] was used to sample at different heights along the centreline of the flame, minimising the perturbation of the flame. The sampling probe has an inner diameter of 8 mm, an outer diameter of 12 mm, and a tip with a pinhole of 0.4 mm. Full details of the sampling system have been reported before [18]. A similar probe has also been reported by Irimiea et al. [38].

The particle size distributions (PSD) were obtained using a Differential Mobility Spectrometer (DMS500) developed and manufactured by Cambustion Ltd. The particles are sized based on their electrical mobility diameter (D_p), which is the diameter of a sphere with the same migration velocity as the particle of interest in a constant electric field [9].

The dilution ratio in the probe was calculated by the DSM500 software and was in the range 150−250 for all experiments. The diluted sample was passed through a conductive silicon tube to the DMS500, where a further dilution by a factor of 500 was achieved with a rotating dilution disc. The total dilution is between the range of 7.5×10^4 – 1.2×10^5. The particle size distribution was measured at a given height from the fuel tube (h) by time-averaging data sampled at a rate of 10 Hz for 20 s. Each experiment was repeated five times. PSD was corrected for the gas expansion inside the flame according to the ideal gas law using the measured gas temperature, and also dilution corrected.

2.3 Soot volume fraction and soot temperature

Two-colour ratio pyrometry was used to obtain the soot volume fraction (f_v) and soot temperature of all the flames. The flame images were recorded with a Blackfly S (FLIR-Integrated Imaging Solutions, Inc.) having a 1/1.8" Sony IMX252 CMOS sensor with 2048×1536 pixels (pixel size 3.45 μm). The camera lens was an MVL25M23 from Thorlabs with an aperture set to f/1.4 and a focal length of 25 mm. The distance between the camera and the flame was 25 cm, resulting in a pixel width corresponding to 1/34 mm in the focal plane through the centre of the flame. A BG-7 filter (Thorlabs) was used to balance the intensity ratios of the three colour channels and to block infrared light. The image processing was performed on single frames to avoid blurring of the flame edges upon averaging. The recently developed Fitting the Line-of-sight Projection of Predefined Intensity Distribution (FLiPPID) methodology was used to perform the inverse Abel transform. This methodology minimises the experimental noise when analysing the projection of axisymmetric coflow diffusion flame images for colour ratio pyrometry. A detailed description of the image processing is given in Dreyer et al. [19].

2.4 Soot sampling and nanostructure analysis

The soot samples were collected using the fast insertion technique in which the soot particles are driven thermophoretically to the cold surface of the substrate [17]. In this case, the rapid insertion of the substrate was achieved using two pull-action computer-controlled solenoids, which allow adjusting the residence time of the probe inside the flame. A similar setup has been reported before [7]. For the Raman spectroscopy analysis, silicon wafer chips (5×5 mm – Agar Scientific) were used as substrate (30 insertions of 40 ms each). The samples for high-resolution transmission electron microscopy (HRTEM) were collected on Holey carbon films (diameter = 3.05 mm – Agar Scientific) on 400 mesh copper grids. The grids were inserted once into the flame for 30 ms.

2.5 Raman spectroscopy

Raman spectra were acquired using a Horiba Jobin-Yvon LabRAM HR spectrometer equipped with a 50x objective and CCD detector. The 532 nm Diode-pumped solid state laser was used to illuminate the samples. The calibration of the system was performed against the Stokes Raman signal of pure Si at 520 cm^{-1} using a silicon wafer. To minimise the possibility of structural changes of the sample due to thermal decomposition by the laser, the power of the excitation laser beam and exposure time were varied to find measurement conditions that avoid the formation of artefacts. Spectra were obtained with a laser beam power of 0.5 mW, and accumulation-exposure times of 3 cycles of 200 s each. At least three samples were collected at each height above the burner, then between 10 to 15 Raman spectra were collected for each sample and averaged to obtain statistically relevant Raman spectra. Subsequently, all the spectra were multipoint baseline corrected and normalised at the G peak around 1600 cm^{-1}using the Origin 2018 package.

2.6 Transmission electron microscopy

HRTEM images were taken using a FEI Tecnai F20 Transmission Electron Microscope with a Gatan digital camera and software with a magnification of 550.000× (59.9502 px/nm). The electron beam was operated at 200 kV for short periods to avoid effects on the internal nanostructure of soot. For the lattice fringe analysis, at least 10 images were analysed. The image processing was performed using the code developed by Botero et al. [7]. In brief, the image processing follows the steps: a) region of interest selection, b) contrast enhancement, c) Gaussian low-pass filter, d) bottom-hat equalisation, e) binarisation using Otsu's method, f) skeletonisation, g) elimination of isolated pixels and pixels with more than three connections. As reported by Botero et al. [7], the fringe length (FL) is calculated as the number of pixels contained by the fringe multiplied by the length of a pixel; all fringes shorter than 0.483 nm (two aromatic rings) are discarded. Fringe tortuosity (τ) is defined as the ratio between the fringe length and the Euclidean distance between the two endpoints of the fringe. The inter-fringe spacing (S) is calculated, taking into account the fringe orientation only fringes with separation between 0.3354 nm and 0.6 nm are accounted for. The parameters used in lattice fringe analysis were chosen to minimise the number of branch points identified and to avoid artificial breaking of the fringes, following a similar procedure to the one reported by Pfau et al. [71].

3 Results

The addition of cyclic fuels to the *n*-heptane coflow diffusion flame increases the visible flame length. The visible flame lengths are reported in Table 1. The addition of cyclic fuels to the *n*-heptane flame results not only in larger visible flame length, but also in a shorter distance between the burner exit and the base of the luminous flame wings and an extended region of yellow luminosity along the centreline, suggesting that soot inception is promoted by the addition of the cyclic fuels and starts earlier in the flame. This is particularly notable in the HEP:20CPE flame, as can be observed in Figure 1.

Figure 2 shows the gas temperature along the centreline for all flames; it also shows the soot temperature calculated by two-colour ratio pyrometry. The gas temperature of the *n*-heptane flame increases monotonically up to 28 mm, reaching a plateau and rising again after 32 mm. The plateau corresponds to the heights at which lower soot temperatures have been observed by two-colour ratio pyrometry. The addition of cyclic fuels produced a significant dip in the temperature centreline profile. Centreline temperature measurements are prone to error in flames with a larger soot concentration, where soot deposition can take place on the thermocouple before reaching the centreline [31, 32, 81, 91]. In our case, the rapid insertion method and extrapolation to time 0 were used to minimise the effect of soot deposition. The transient thermocouple response in regions with high soot concentration can be observed in (Figure SM1).

Nevertheless, the gas thermocouple measurement and the soot temperature results show that the dips are correlated with temperature losses in the flame through radiative heat loss. There is a correlation between soot temperature and gas temperature is observed in Figure 2, in which the centerline gas temperature dips are located in the region of lower

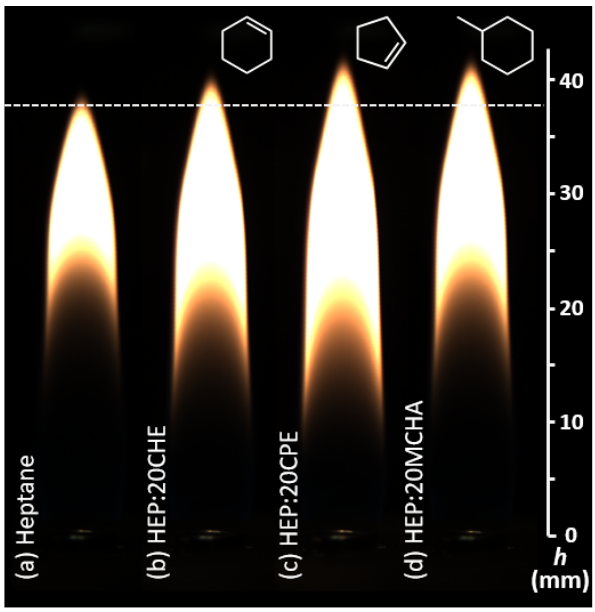

Figure 1: *Photographs of the coflow diffusion flames studied. In all the cases, the exposure and colour balance ratio were kept constant.*

soot temperature in all the flames. Radiative heat loss is known to be enhanced with increasing fuel sooting propensity [16, 51]. This can be observed in the gas and soot temperature results.

3.1 Particle size distribution and soot volume fraction

Figure 3 shows the PSD measured at different heights above the burner for all the investigated flames. The observed mobility diameter of the particles is in the range between 10 and 300 nm. For each flame, the particle size distribution was measured along the centreline from 10 mm above the fuel tube to the flame tip.

The different values of heights shown in Figure 3 allow the soot particle growth process to be followed (Figure 3a - c). The average particle size for *n*-heptane increases from 8.5 mm at h= 16 mm to 24 nm at h= 24 mm. The presence of a bimodality is detected at 28 mm (Figure 3d). The maximum size of the agglomeration mode is reached at 32 mm (Figure 3e). This can also be observed from the average particle size Figure SM4, in which the maximum particle diameter is reached at 32 mm. After that, the oxidation of the particles is observed, and the average particle size starts to decrease (Figures 3f and SM4).

The addition of cyclic fuels increases the number of particles detected early in the flame (Figure 3a), as well as the particle size. This suggests that the addition of the cyclic fuels promotes the particle formation at lower height in the flame. The first particles were detected at h=15 mm in the *n*-heptane flame, whereas in the HEP:20CPE the first particles were detected at h=11 mm. This can be related to the formation of aromatic species such as benzene and small PAH at higher rates than in *n*-heptane flames. The fuels with double

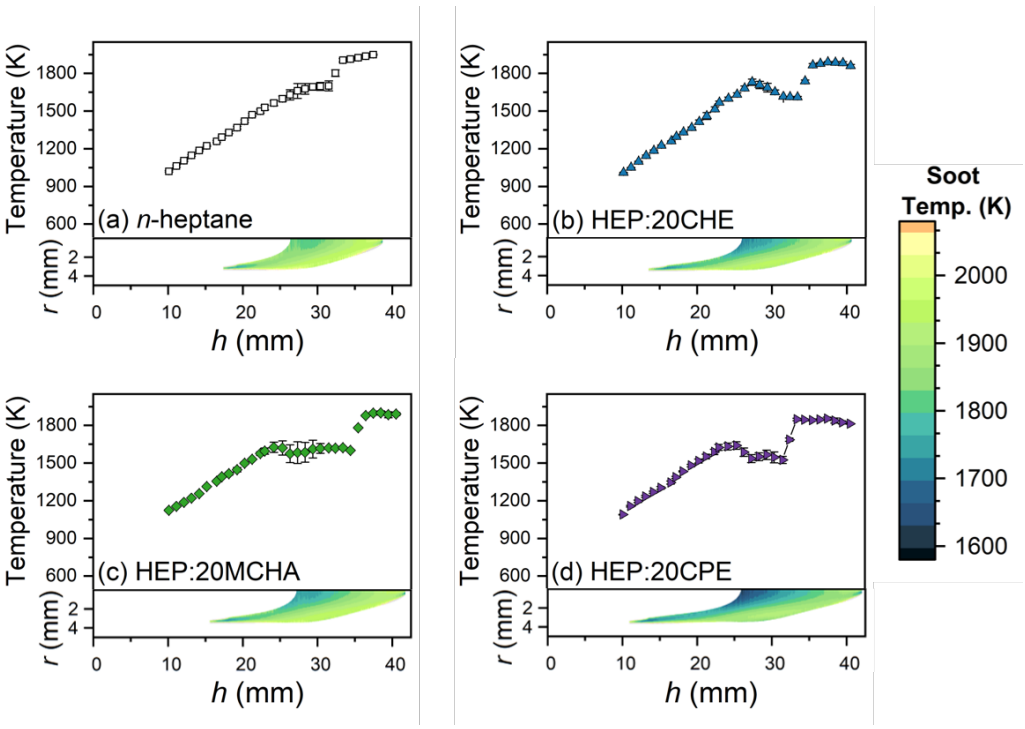

Figure 2: *Temperature centreline profiles for (a) n-heptane, (b) HEP:20CHE, (c) HEP:20MCHA, and (d) HEP:20CPE coflow diffusion flames, including soot temperature obtained by two-colour ratio pyrometry. r is the radial distance from the flame centerline. The error bars indicate the standard error of the measurements, several of the errors bars are smaller than the symbols.*

bonds (cyclohexene and cyclopentene) more strongly promote soot formation, as expected from their sooting tendency [57]. Figure SM2 shows the evolution of the PSD for each flame at different heights, so it is easier to see the evolution of the PSD for the different fuels.

The soot volume fraction (f_v) (Figure 4) and soot temperature (Figure SM3) were determined using two-colour ratio pyrometry. The maximum soot volume fraction for *n*-heptane is around 1.0 ppm. A similar value has been reported before [19, 41]. In all the cases, the soot volume fraction increases with the addition of cyclic fuels. The level of increase of the soot volume fraction is a function of the fuel structure. A 5-membered ring (cyclopentene) promotes a higher increase in soot volume fraction than a 6-membered ring (cyclohexene). The addition of 20% of cyclopentene increased the soot volume fraction by a factor of 2. The significant increase in the particle size and soot volume fraction suggests a synergistic effect between the species present in the *n*-heptane flame and the species produced by the cyclic fuels decomposition pathways, as it will be discussed in Section 4.

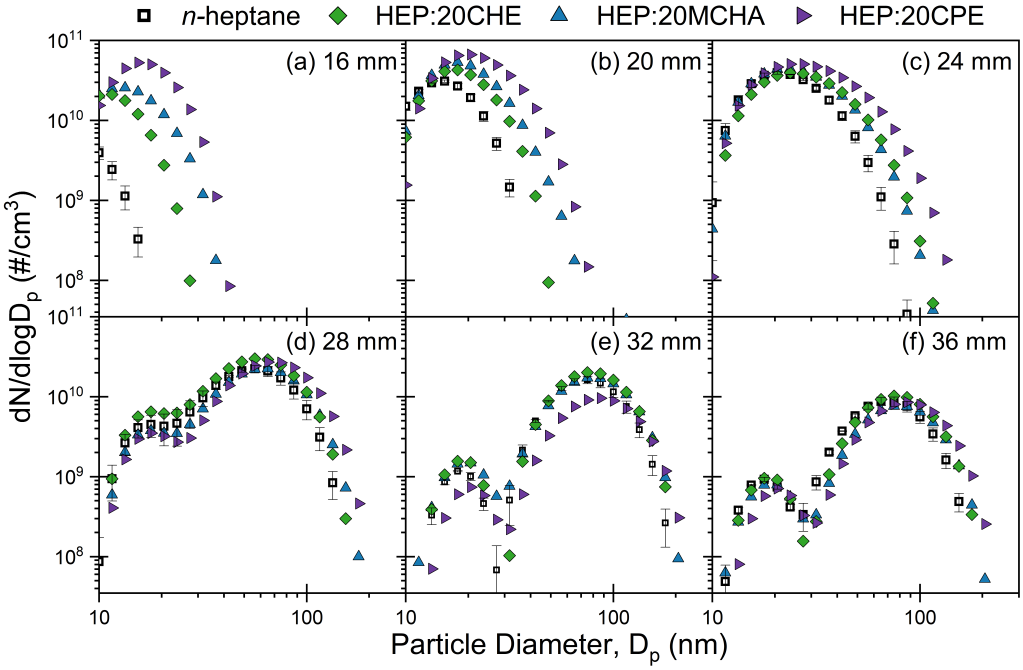

Figure 3: *Comparison of the particle size distribution at different heights from the tube fuel exit for n-heptane, HEP:20CHE, HEP:20CPE, and HEP:20MCHA coflow diffusion flames. The error bars indicate the standard error of the measurements. For all the other PSDs, the error bars are similar but are not shown to retain clarity of presentation.*

3.2 Particle nanostructure

3.2.1 Raman spectroscopy

Samples for Raman spectroscopy were collected at two different heights in the flames, to compare particles with similar mobility diameters that were not undergoing oxidation. For this reason, particles with an average particle diameter of 25 and 80 nm were sampled. The particles with an average particle size of 25 and 80 nm are observed at $h = 22$–25 mm and $h = 30$–33 mm, respectively (Figure SM4). In this study, we used Raman spectroscopy to obtain structural information from the soot. Figure 5 shows the spectra obtained for samples collected in the HEP:20CPE flame with an average particle size of (a) 25 nm, and (b) 80 nm. The spectra for all the samples are presented in Figure SM5. In all cases, the spectra exhibit two broad and strong overlapping peaks: The organised graphite-like carbon or G band (~ 1580 cm^{-1}), and the D band associated with the nature of disordered graphite (~ 1345 cm^{-1}). The G band is attributed to the ideal graphitic lattice vibration mode (E_{2g} symmetry) [82]. The D band is associated with the graphitic lattice breathing mode (A_{1g} symmetry) [23], which is forbidden in the ideal graphitic lattice and becomes active only in the presence of disorder or defects. The particles collected at h= 25 nm exhibit a photoluminescent background related to the high hydrogen content in the sample (Figure 5).

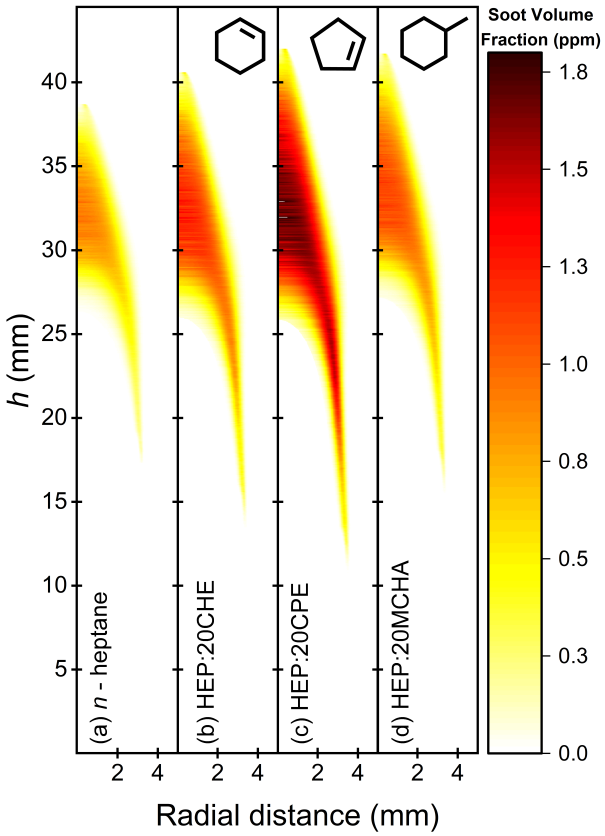

Figure 4: *Soot volume fraction obtained by colour ratio pyrometry of (a) n-heptane, (b) HEP:20CPE, (c) HEP:20CHE, and (d) HEP:20MCHA coflow diffusion flames.*

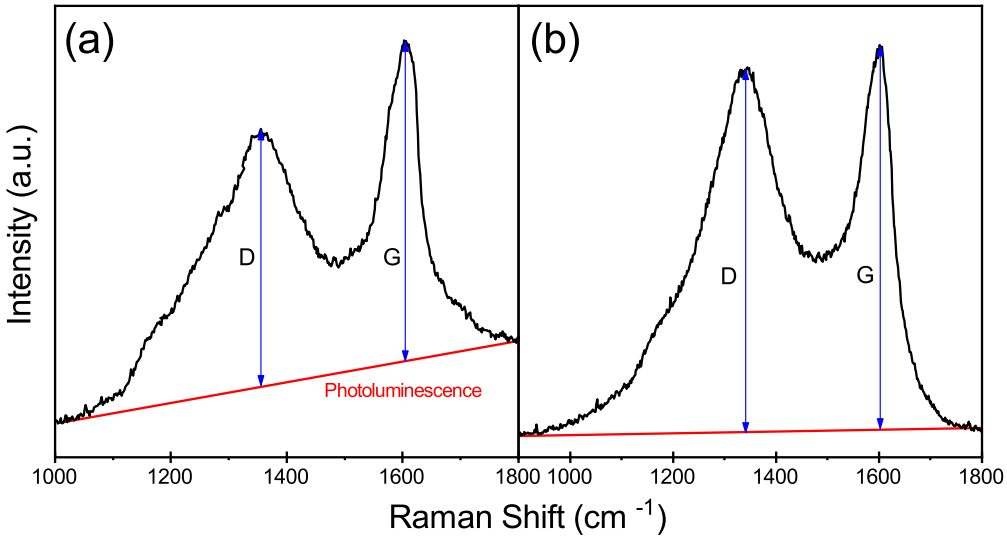

Figure 5: *Raman spectra for samples collected in the HEP:20CPE with an average particle size of (a) 25 nm, and (b) 80 nm.*

The correlation developed by Ferrari and Robertson [21, 23], and based on previous works

[45, 82], was used to calculate crystallite size L_a, as shown in equation 1. It has been theoretically and experimentally determined, that for a nanocrystallite, I(G) is proportional to the sample area, whereas I(D) is produced only by a small region of the crystal near a defect or an edge, and it is proportional to the overall length of the edge, which scales as L_a [22]:

$$\frac{I(\mathrm{D})}{I(\mathrm{G})} = C'(\lambda)L_a^2 \tag{1}$$

where $C'(\lambda)$ is a wavelength-dependent pre-factor. The $I(D)/I(G)$ ratio was calculated after baseline correction and normalisation of the spectra by the intensity of the G band, as shown in Figure 5. Table 2 reports the L_a values calculated for the sample collected for all the fuels. It is evident that L_a increases as function of height from the fuel tube, which is related to the particle and fringe growth. Similar values for L_a are obtained for all the fuels at a given height.

Table 2: *Hydrogen content and crystallite size for particles with an average particle size of 25 nm (h=22–25 mm) and 80 nm (h=30–33 mm)*

Flame	Particle diameter		
	25 nm		80 nm
	H (at%)	L_a (nm)	L_a (nm)
n-heptane	34 ± 2	1.22 ± 0.03	1.28 ± 0.02
HEP:20CHE	35 ± 1	1.24 ± 0.01	1.25 ± 0.01
HEP:20CPE	31 ± 4	1.23 ± 0.02	1.31 ± 0.02
HEP:20MCHA	34 ± 2	1.21 ± 0.02	1.25 ± 0.01

Similarly, H (at %) content was calculated following the correlation developed by Casiraghi et al. [10]:

$$H[\mathrm{at\%}] = 21.7 + 16.6 \log\left\{\frac{m}{I(\mathrm{G})}[\mu\mathrm{m}]\right\} \tag{2}$$

where m is the slope of the photoluminiscent background, measured for the baseline between 1000 and 1800 cm^{-1} and I(G) corresponds to the intensity of the G band. The results are shown in Table 2. This simple method allows the estimation of the hydrogen content in a small amount of sample compared to other methods that require larger sample quantities. In all the cases, the atomic hydrogen content is around 34%, leading to an H/C ratio of 0.5. This H/C ratio is characteristic for newly incepted particles (young soot) and decreases as the carbonisation process takes place along the flame [76]. The atomic hydrogen content was not calculated for the samples with an average particle size of 80 nm because the hydrogen content is low and the spectra do not exhibit a photoluminescent background, as can be observed in Figure SM5.

3.2.2 Transmission electron microscopy

The HRTEM images were processed as described by Botero et al. [7]. Figure 6 shows some representative high resolution images collected at $h = 32$ mm in the different flames. The samples were collected at this height to allow the inception and growth of the particle, but before undergoing the oxidation process to understand the changes induced by the addition of cyclic fuels on the soot nanostructure. A concentric orientation of fringes, onion-like, structure is recognisable in all the particles, with an disordered core and a shell with graphitic-like domains formed by the graphitisation or annealing of the particles [2, 84].

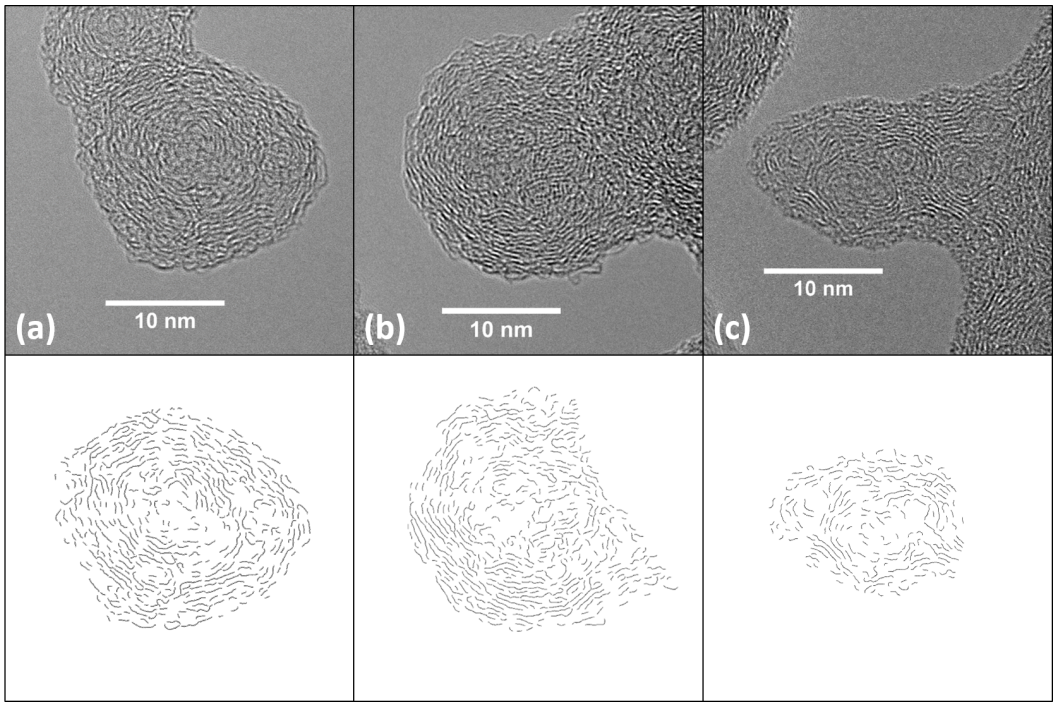

Figure 6: *Skeletonized (Bottom row) and unprocessed HRTEM images (Upper row) of primary carbon nanoparticulates collected in (a) n-heptane, (b) HEP:20CHE, (c) HEP:20CPE coflow diffusion flames at* $h = 32$ mm.

The fringe length, fringe tortuosity and inter-fringe spacing were calculated as described in Section 2.6 to understand the effect of the cyclic fuels on the soot formation in the doped *n*-heptane flames. The results obtained from the analysis of all the images were used to calculate the median of the fringe length (FL), fringe tortuosity (τ) and inter-fringe spacing (S). The distributions of the full set of data obtained for each parameter are presented in Figure SM6. The results are summarised in Table 3. The median values for the fringe length, fringe tortuosity and inter-fringe spacing suggest that the addition of cyclohexene to *n*-heptane does not induce significant changes in the soot nanostructure. Moreover, cyclopentene promotes the formation of shorter and more tortuous fringes.

Recently, Botero et al. [8] have reported that most of the fringes in soot, from a coflow diffusion flame, are almost flat ($\tau < 1.15$), or present a low degree of curvature ($1.15 < \tau < 1.35$), with only a small proportion of highly curved fringes ($\tau > 1.35$). The percentages corre-

Table 3: *Experimental medians for fringe length (FL), fringe tortuosity (τ) and inter-fringe spacing (S) obtained from the image analysis of the particles collected at $h = 32$ mm. The medians are calculated across the full set of data obtained for each parameter.*

Flame	FL (nm)	τ	S (nm)
n-heptane	0.936	1.13	0.414
HEP:20CHE	0.903	1.14	0.418
HEP:20CPE	0.834	1.16	0.414

sponding to each range were calculated for the full set of data, the results are presented in Table 4. It is evident that most of the fringes present a low degree of curvature. Nevertheless, the addition of cyclopentene to *n*-heptane flame increases the proportion of fringes with $\tau > 1.35$ indicating the presence of highly curved fringes. The incorporation of 5- or 7-membered rings in the PAHs has been suggested as the main reason for the curvature observed in the fringes [29, 72, 95], and it has been suggested that a low curvature is related to the presence of a maximum one or two pentagonal rings in the PAH [2]. Recently, Martin et al. [54] have simulated the TEM images of different kinds of PAH with a fringe length of $\sim$1 nm. They found that small cross-linked PAHs could produce tortuous fringes; however, the maximum fringe tortuosity that could originate from a PAH cross-linked species was $\tau = 1.15$, a value similar to τ of a curved PAH with a single pentagonal ring. Therefore, tortuosity values > 1.15 are considered to be predominantly due to the integration of five-membered rings and not cross-linked species. This indicates that the higher proportion of fringes with a $\tau > 1.35$ is related to the incorporation of five-membered rings in the PAH nanostructure indicating that cyclopentene addition to *n*-heptane promotes the formation of cPAHs.

Table 4: *Fringe tortuosity (τ) of the particles collected at $h = 32$ mm. The percentages show the proportion of the population of fringes with tortuosity in each interval.*

Flame	$\tau < 1.15$ (%)	$1.15 < \tau < 1.35$ (%)	$\tau > 1.35$ (%)
n-heptane	52.8	34.9	12.3
HEP:20CHE	52.1	36.3	11.6
HEP:20CPE	40.6	40.7	18.7

4 Discussion

Figure 7 shows what are believed to be the main formation pathways of key intermediates in the soot formation process (benzene, fulvene and cyclopentadiene) from cyclohexene, cyclopentene and methylcyclohexane. The formation of the first aromatic ring takes place through different reactions for each fuel. This scheme is mainly based on decomposition

pathways reported in the literature for pyrolysis or coflow diffusion flame experiments [4, 34, 48, 59–61, 64, 65, 80, 83, 92].

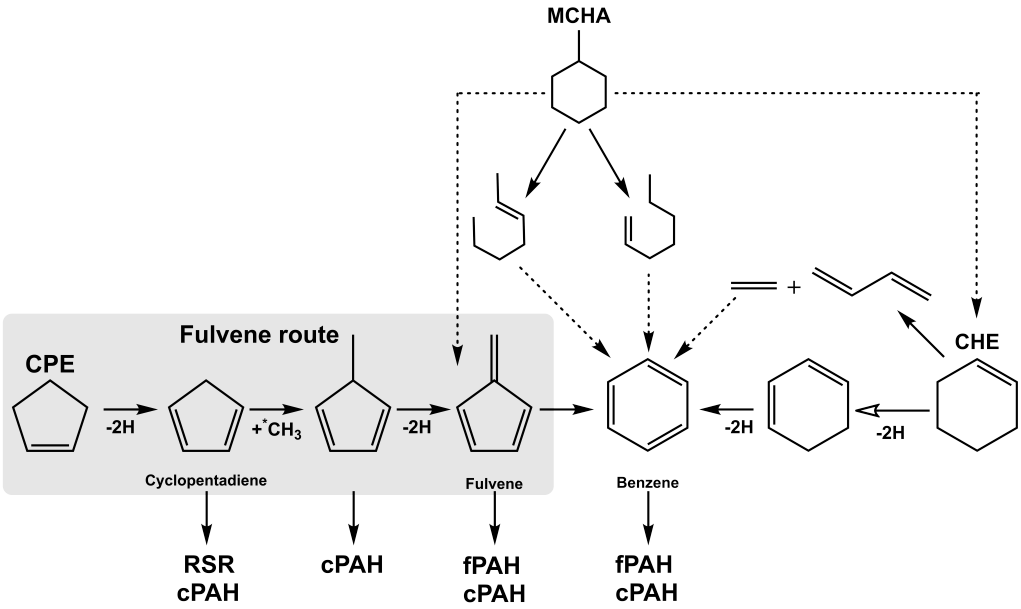

Figure 7: *Scheme of possible reaction pathways and key intermediates for soot formation in coflow diffusion flames from cyclohexene (CHE), methylcyclohexane (MCHA) and cyclopentene (CPE). Dash arrows indicate reactions involving different intermediate species, hollow arrowhead indicate reactions with low probability to occur at flame conditions. No radical species were included to simplify the illustration. The gray box shows the fulvene route. RSR = Resonance Stabilised Radicals, cPAHs = curve polycyclic aromatic hydrocarbons, fPAHs = flat aromatic hydrocarbons.*

The *n*-heptane decomposition pyrolysis main products are H_2 and C_nH_{2n} due to C-C bond cleavage reactions which have a low barrier for unimolecular decomposition [97]. A significant production of C_2H_4 has been observed in methane coflow diffusion flames doped with *n*-heptane [63]. This suggests that C-C bond cleavage reactions are also important in coflow diffusion flames. Modelling results for coflow diffusion flames showed that benzene is mainly formed through the reactions shown in Equations 3 and 4 [13, 50]. It has been found that fulvene chemistry is important for the benzene formation in *n*-heptane rich premixed flames [79]. However, fulvene has not been taken into account as a key species in benzene formation in the modelling of *n*-heptane coflow diffusion flames [13, 50].

$$C_3H_3 + C_3H_3 \longleftrightarrow \text{Benzene} \tag{3}$$

$$n\text{-}C_4H_5 + C_2H_2 \longleftrightarrow \text{Benzene} + H \tag{4}$$

Different pyrolysis studies for cyclohexene established that the main products are ethene and 1,3-butadiene with small amount of 1,3-cyclohexadiene and traces of 1,4-cyclohexadiene and benzene. Thus, the main decomposition path is a retro-Diels-Alder reaction [4, 80, 83, 89] instead of successive dehydrogenation reactions (Figure 7). It has been proposed that a small amount of cyclohexadienes are formed from cyclohexene, and the cyclohexadienes contribute more than 80% to benzene formation [89]. These findings are in good agreement with McEnally and Pfefferle [59]; they also found a significant amount of ethene and C4 species proposed in methane coflow diffusion flames doped with cyclohexene. However, they suggest that cyclohexene dehydrogenation has a role in benzene formation because benzene concentration does not exhibit a linear correlation with C_3H_4 species.

It is accepted that the main decomposition pathway for cyclopentene is a hydrogen elimination to form cyclopentadiene (Figure 7). This species has been experimentally detected in coflow diffusion flames [61], low-pressure premixed flames [48] and pyrolysis [34]. Cyclopentadiene can transform into benzene through the fulvene route (Figure 7). Additionally, experimental evidence established the cyclopentadienyl radical as an important intermediate in PAH formation because its ability of self-recombination where PAHs, such as naphthalene, are formed without benzene as an intermediate [34, 48, 65]. In addition, cyclopentene can promote different pathways to form Resonance Stabilised Radicals (RSR) [40], cPAHs [94], among others.

Substituted cyclohexanes, as methylcyclohexane, mainly decompose by unimolecular dissociation in coflow laminar flames. The primary dissociation reaction is the ring-opening isomerisation, as shown in Figure 7. The 1-heptene and 2-heptene formed can decompose through allylic C-C fission (high temperature) or/and 6-centred elimination (low temperature) depending on the flame conditions [60]. These lead to the formation of C2, C3 and C4 species which are important for benzene formation [64, 92].

As described above, the cyclic fuels used in this study are able to form small aromatics rings via different pathways. The addition of cyclic fuels results in the first aromatic ring forming more quickly than in pure aliphatic flames (*n*-heptane). Cyclopentene primarily forms benzene via the fulvene route, whereas cyclohexene and methylcyclohexane primarily form benzene through recombination reactions. In addition, a small proportion of cyclohexene also forms benzene via dehydrogenation reactions. In addition, the high concentration of small species (C1-C4) in *n*-heptane coflow diffusion flames [50, 63] promotes the growth of PAHs driven by H-Abstraction-Acetylene-Addition (HACA) [88] or similar mechanisms [30, 75, 90]. Therefore, the addition of cyclic fuels, keeping constant the total amount of carbon, has a synergistic effect leading to larger particles and more soot, as has been observed in the soot volume fraction and particle size distribution results, Figures 3 and 4, respectively.

In this case, HRTEM results suggested that the percentage of highly curved fringes ($\tau > 1.35$) increased by the addition of cyclopentene (Tables 3 and 4). This is related to the incorporation of five-membered rings in PAHs, which has been computationally [25, 85, 93, 96] and experimentally [12, 29, 40, 78] studied. Johansson et al. [40] have suggested the key role of Resonance-Stabilised Radicals in the formation of soot, in which radicals such as vinylcyclopentadienyl are important intermediates in the formation of five-membered ring species as indenyl or fluorenyl radical. In addition, structures containing between

5- to 16- aromatic rings with different kinds of moieties incorporating pentagonal rings in their structure have been identified by Atomic Force Microscopy (AFM) [12, 78]. As has been explained before, the decomposition pathways of cyclohexene do not suggest a significant amount of cyclopentadienyl radicals formed in coflow diffusion flames, and a lower amount of five-membered rings are going to be formed than with cyclopentene. This is correlated with the similar values for fringe length and fringe tortuosity observed for soot collected from *n*-heptane flames doped with cyclohexene.

There are different possible pathways in which the addition of cyclopentene can contribute to soot formation after increasing the proportion of five-membered rings incorporated in the cPAH and soot. The incorporation of five-membered rings implies a permanent dipole moment due to the flexoelectric effect, which can increase clustering among cPAH or with chemi-ions [53, 54]. The promotion of the clustering of hydrocarbons by radical-chain reactions mechanism as proposed by Johansson et al. [40], in which cyclopentadienyl (from the cyclopentene) and small hydrocarbons (from *n*-heptane) as ethene an ethyne are key elements in the soot inception process; and the clustering of localised π-radicals, which have been suggested as important species in soot nucleation due to their significant binding energy and the potential to rapidly generate them via protonation of abundant rim-based pentagonal rings [55]. It will be necessary to perform more experiments to know precisely how the cyclopentene addition changes the soot inception process in *n*-heptane coflow diffusion flames.

Apart from fundamental insights into the formation of soot, the integration of curvature is also of significant interest to industrial carbons such as carbon blacks. For catalytic applications, curved carbons have been found to have an enhanced catalytic activity for chlorination [11]. This reactivity has been rationalised as the attachment and reaction of the convex surface with chlorine. Similarly, increased reactivity towards oxygen was found with computational work revealing an increased edge reactivity towards oxygen [74]. For adsorption applications, curvature integration could allow for tuning the flexoelectric dipole moment in these materials. This effect has been shown to impact hydrogen adsorption [77], and storage of lithium [98], both of considerable interest for energy storage. To date curvature integration has primarily relied on the addition of oxygen concentration within partially premixed flames [36]. However, the addition of cyclopentene to coflow diffusion flames is one of the first examples of a non-oxidative route to integrating curvature. Therefore, it could be of importance for integrating curvature in carbons for applications where oxygen needs to be kept to a minimum for example in electronic applications, e.g. batteries.

5 Conclusions

This paper has investigated changes induced by the addition of cyclic fuels in an *n*-heptane laminar coflow diffusion flame. The flame structure was studied by two-colour ratio pyrometry to calculate the soot volume fraction and soot temperature, differential mobility spectrometry for particle size distribution determination, and gas temperature measurements by thermocouple. The soot nanostructure was investigated using Raman spectroscopy and lattice-frince analysis of high-resolution transmission electron microscopy.

The addition of partially unsaturated cyclic fuels promotes the formation of soot in *n*-heptane coflow diffusion flames. The presence of a double-bond in the cyclic fuel has a larger effect than a methyl substitution. The particle size distribution measurements and the colour-ratio pyrometry results suggest that cyclopentene promotes soot inception earlier in the flame, leading to larger particle size and higher soot volume fractions in the flame, and possibly because of promoting the clustering of hydrocarbons through different mechanisms.

Raman spectroscopy results indicate there is no significant difference in hydrogen content even when different cyclic fuels are present in the flame. Nevertheless, HRTEM results suggest a significant influence of the cyclopentene on the soot nanostructure. The fringe analysis shows an increase in the fringe tortuosity when cyclopentene is added to *n*-heptane, and it is related to the incorporation of five-membered rings in the soot fringes structure. This suggests cyclopentene could be used as a fuel to incorporate curvature in different carbonaceous structures to modify their properties.

Acknowledgements

This project is supported by the National Research Foundation (NRF), Prime Minister's Office, Singapore under its Campus for Research Excellence and Technological Enterprise (CREATE) programme. The authors would like to thank the European Unions Horizon 2020 Research and Innovation Programme under grant agreement no. 724145. We thank Prof. Alexei Lapkin of the Department of Chemical Engineering and Biotechnology of the University of Cambridge for allow us to use the Raman spectrometer.

Competing interests

The authors have no competing interests to declare.

Supplementary information

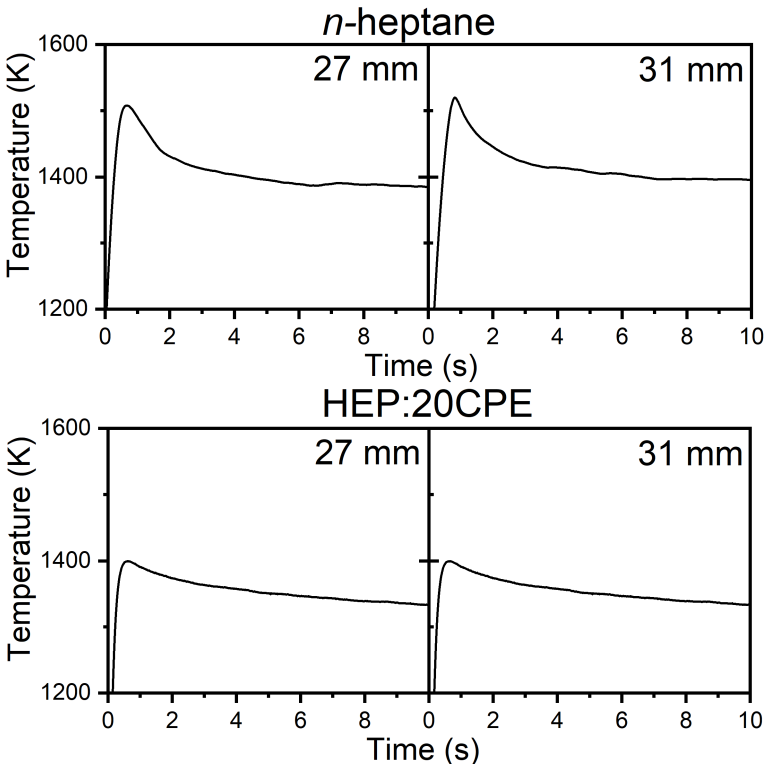

Figure SM1: *Measured temperature as function of time in regions with high soot concentrations.*

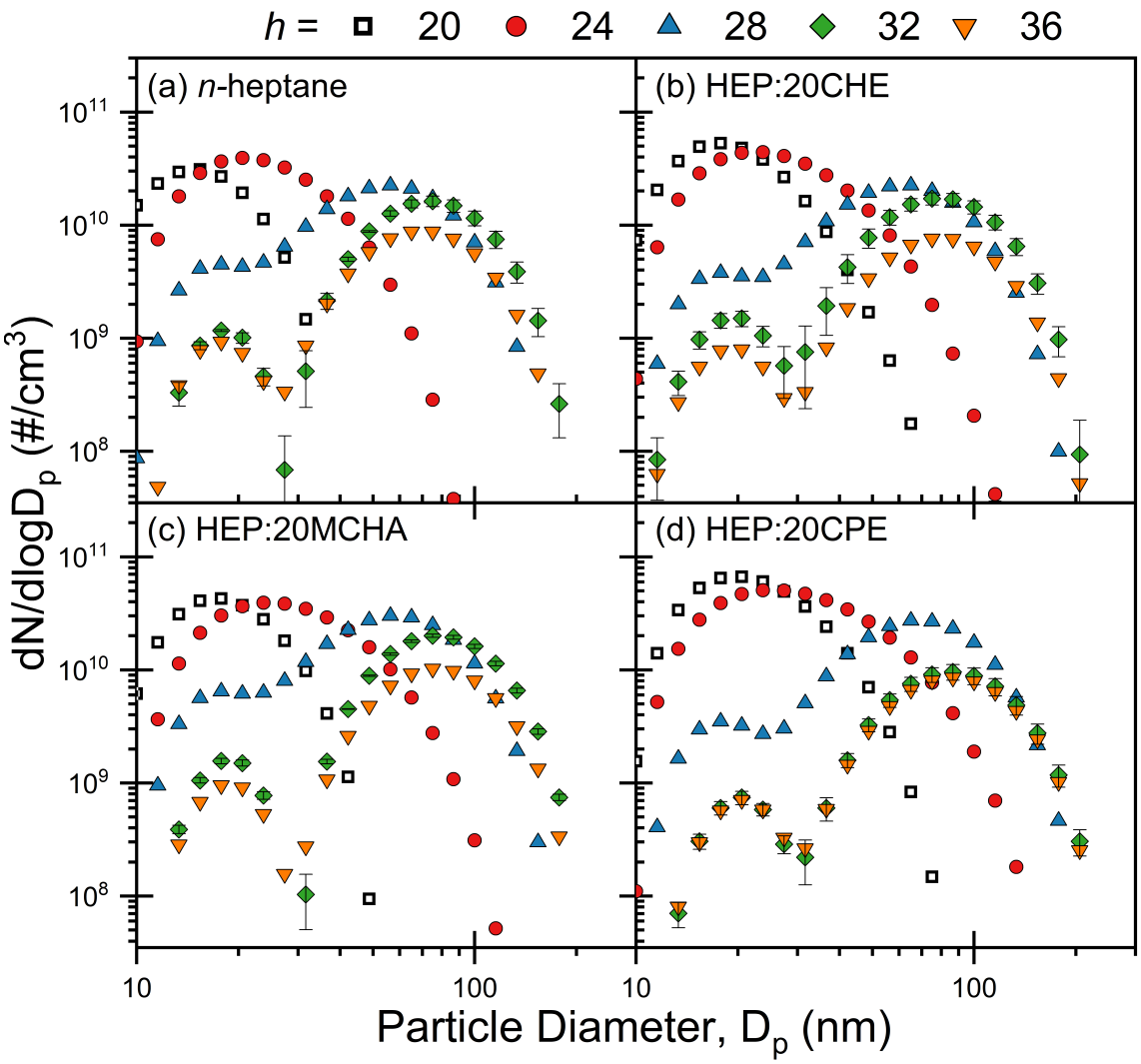

Figure SM2: *Particle size distribution in coflow diffusion flames of (a) n-heptane, (b) HEP:20CHE, (c) HEP:20MCHA, and (d) HEP:20CPE coflow diffusion flames. The error bars indicate the standard error of the measurements. For all the other PSDs, the error bars are similar but are not shown to retain clarity of presentation.*

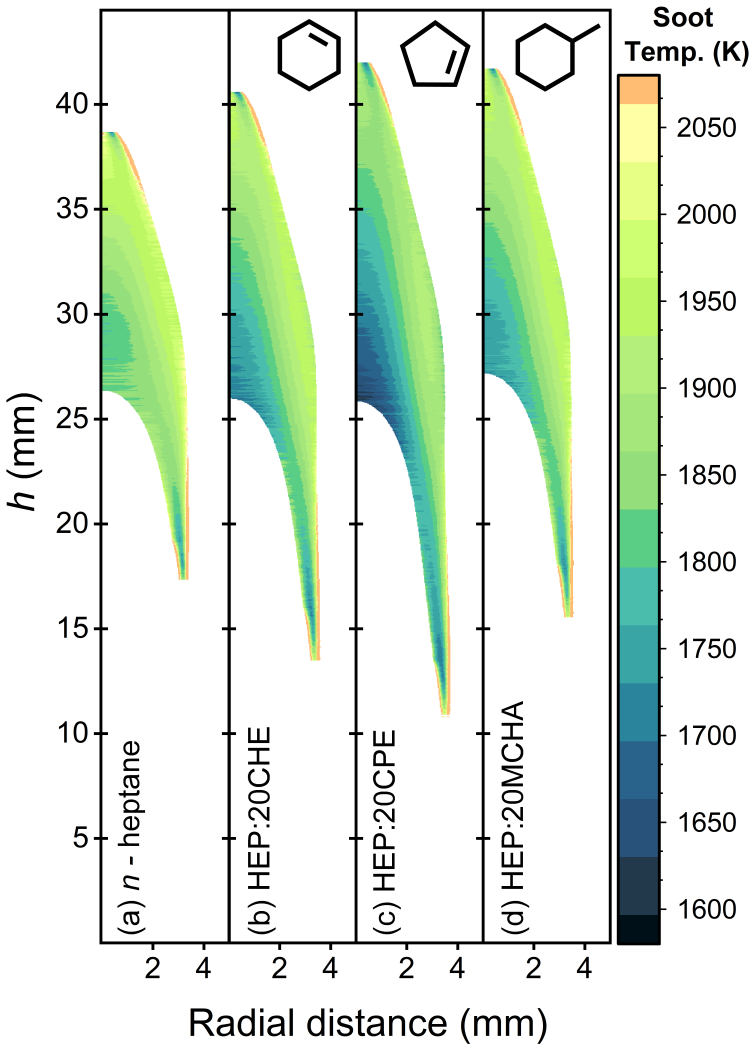

Figure SM3: *Soot temperature in coflow diffusion flames of (a) n-heptane, (b) HEP:20CHE, (c) HEP:20CPE, and (d) HEP:20MCHA.*

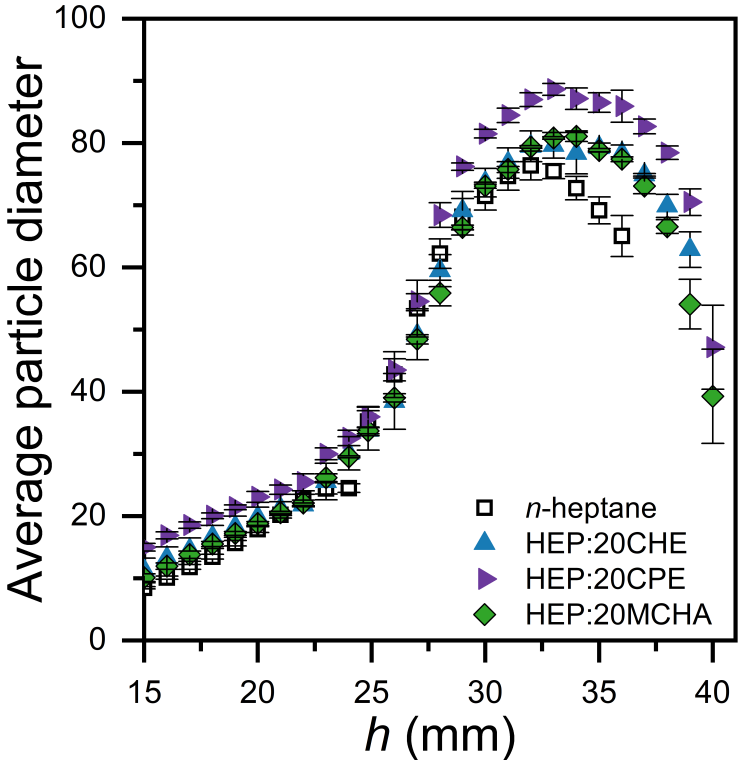

Figure SM4: *Average particle size along the centerline of coflow diffusion flames of n-heptane, HEP:20CHE, HEP:20MCHA, and HEP:20CPE. The error bars indicate the standard error of the measurements. For all the other PSDs, the error bars are similar but are not shown to retain clarity of presentation.*

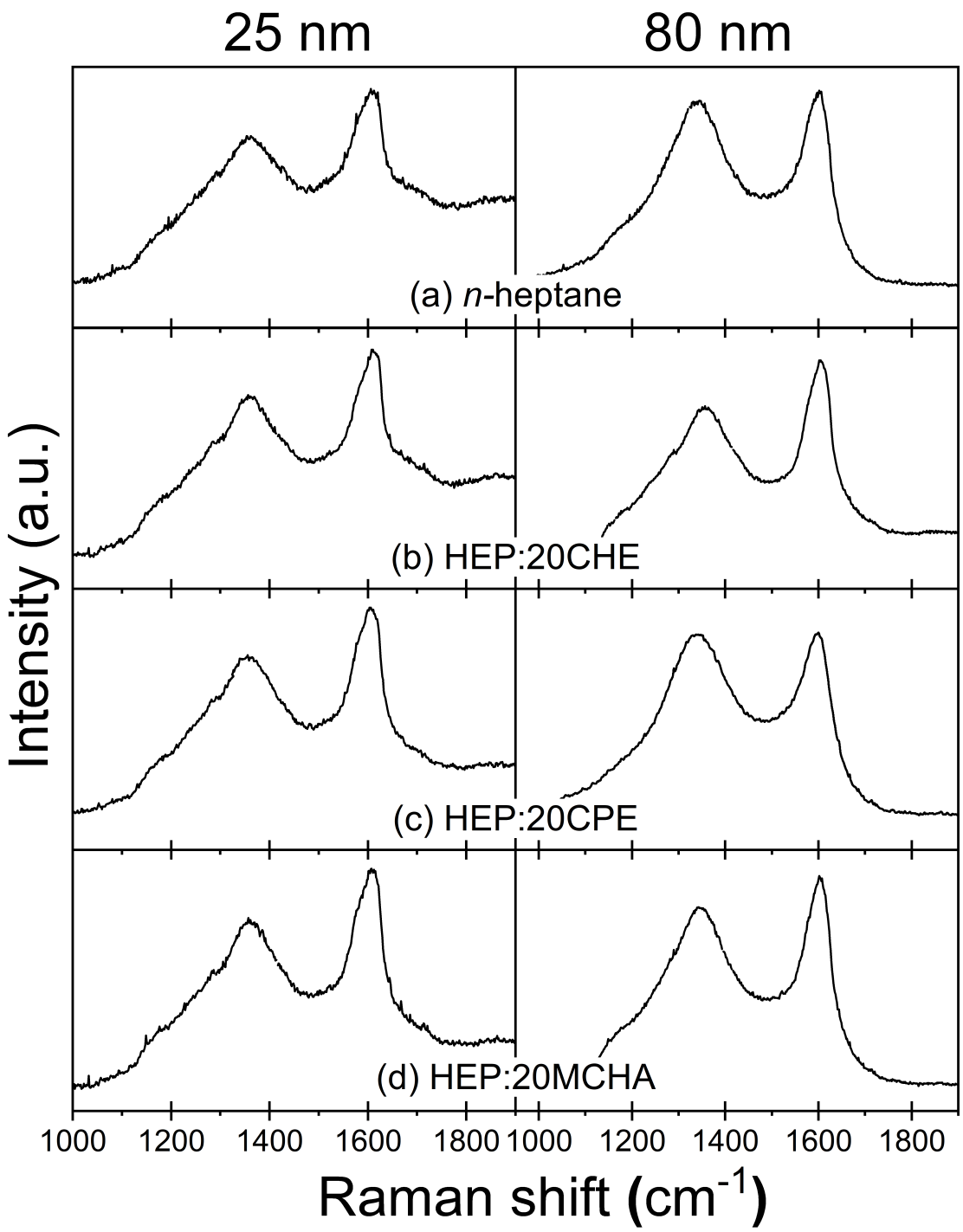

Figure SM5: *Raman spectra for samples collected in (a) n-heptane, (b) HEP:20CHE, (c) HEP:20CPE, and (d) HEP:20MCHA with an average particle size of 25 nm (left column), and (b) 80 nm (right column).*

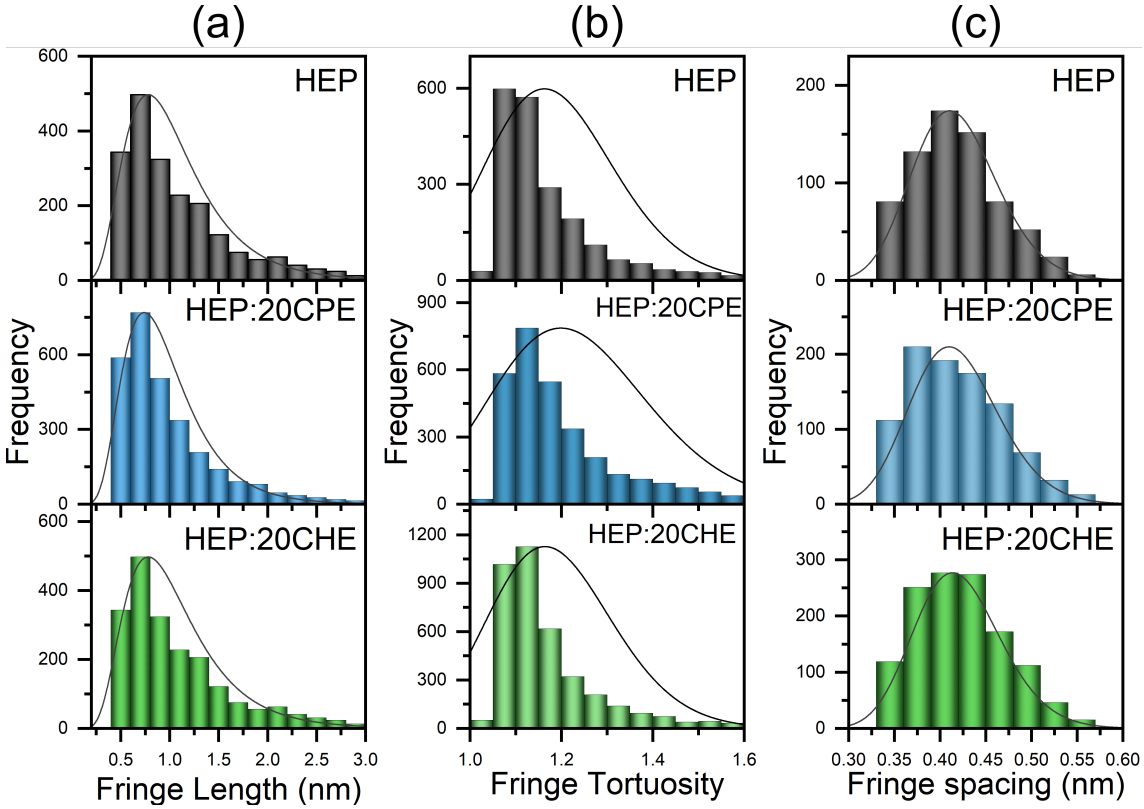

Figure SM6: *Histograms of (a) fringe length, (b) fringe tortuosity and (c) inter-fringe spacing of soot generated from a n-heptane, HEP:20CPE, and HEP:20CHE flames collected at $h = 32$ mm. The histograms show the full set of data obtained for each parameter. Lines represent a lognormal distribution curve to guide the eye.*

References

[1] R. K. Abhinavam Kailasanathan, T. L. Yelverton, T. Fang, and W. L. Roberts. Effect of diluents on soot precursor formation and temperature in ethylene laminar diffusion flames. *Combustion and Flame*, 160(3):656–670, 2013. doi:10.1016/j.combustflame.2012.11.004.

[2] B. Apicella, P. Pré, M. Alfè, A. Ciajolo, V. Gargiulo, C. Russo, A. Tregrossi, D. Deldique, and J. N. Rouzaud. Soot nanostructure evolution in premixed flames by High Resolution Electron Transmission Microscopy (HRTEM). *Proceedings of the Combustion Institute*, 35(2):1895–1902, 2015. doi:10.1016/j.proci.2014.06.121.

[3] R. W. Atkinson, S. Kang, H. R. Anderson, I. C. Mills, and H. A. Walton. Epidemiological time series studies of PM2.5 and daily mortality and hospital admissions: A systematic review and meta-analysis. *Thorax*, 69(7):660–665, 2014. doi:10.1136/thoraxjnl-2013-204492.

[4] J. A. Barnard and T. K. Parrott. Kinetics of the thermal unimolecular reactions of cyclohexene and 4-vinylcyclohexene behind reflected shockwaves. *Journal of the Chemical Society, Faraday Transactions 1: Physical Chemistry in Condensed Phases*, 72:2404–2415, 1976. doi:10.1039/F19767202404.

[5] D. Bartos, M. Sirignano, M. J. Dunn, A. D'Anna, and A. R. Masri. Soot inception in laminar coflow diffusion flames. *Combustion and Flame*, 205:180–192, 2019. doi:10.1016/j.combustflame.2019.03.026.

[6] T. C. Bond, S. J. Doherty, D. W. Fahey, P. M. Forster, T. Berntsen, B. J. Deangelo, M. G. Flanner, S. Ghan, B. Kärcher, D. Koch, S. Kinne, Y. Kondo, P. K. Quinn, M. C. Sarofim, M. G. Schultz, M. Schulz, C. Venkataraman, H. Zhang, S. Zhang, N. Bellouin, S. K. Guttikunda, P. K. Hopke, M. Z. Jacobson, J. W. Kaiser, Z. Klimont, U. Lohmann, J. P. Schwarz, D. Shindell, T. Storelvmo, S. G. Warren, and C. S. Zender. Bounding the role of black carbon in the climate system: A scientific assessment. *Journal of Geophysical Research Atmospheres*, 118(11):5380–5552, 2013. doi:10.1002/jgrd.50171.

[7] M. L. Botero, D. Chen, S. González-Calera, D. Jefferson, and M. Kraft. HRTEM evaluation of soot particles produced by the non-premixed combustion of liquid fuels. *Carbon*, 96:459–473, 2016. doi:10.1016/j.carbon.2015.09.077.

[8] M. L. Botero, Y. Sheng, J. Akroyd, J. Martin, J. A. Dreyer, W. Yang, and M. Kraft. Internal structure of soot particles in a diffusion flame. *Carbon*, 141:635–642, 2019. doi:10.1016/j.carbon.2018.09.063.

[9] Cambustion Ltd. DMS500 Fast Particulate Analyzer - user manual. Technical report, Cambridge, United Kingdom, 2015. URL `www.cambustion.com`.

[10] C. Casiraghi, F. Piazza, A. C. Ferrari, D. Grambole, and J. Robertson. Bonding in hydrogenated diamond-like carbon by Raman spectroscopy. *Diamond and Related Materials*, 14(3-7):1098–1102, 2005. doi:10.1016/j.diamond.2004.10.030.

[11] G. Centi, K. Barbera, S. Perathoner, N. K. Gupta, E. E. Ember, and J. A. Lercher. Onion-like graphene carbon nanospheres as stable catalysts for carbon monoxide and methane chlorination. *ChemCatChem*, 7(18):3036–3046, 2015. doi:10.1002/cctc.201500662.

[12] M. Commodo, K. Kaiser, G. De Falco, P. Minutolo, F. Schulz, A. D'Anna, and L. Gross. On the early stages of soot formation: Molecular structure elucidation by high-resolution atomic force microscopy. *Combustion and Flame*, 205:154–164, 2019. doi:10.1016/j.combustflame.2019.03.042.

[13] J. L. Consalvi and F. Liu. Numerical study of the effects of pressure on soot formation in laminar coflow *n*-heptane/air diffusion flames between 1 and 10 atm. *Proceedings of the Combustion Institute*, 35(2):1727–1734, 2015. doi:10.1016/j.proci.2014.07.045.

[14] A. D'Anna. Combustion-formed nanoparticles. *Proceedings of the Combustion Institute*, 32(1):593–613, 2009. doi:10.1016/j.proci.2008.09.005.

[15] D. D. Das, W. J. Cannella, C. S. McEnally, C. J. Mueller, and L. D. Pfefferle. Two-dimensional soot volume fraction measurements in flames doped with large hydrocarbons. *Proceedings of the Combustion Institute*, 36(1):871–879, 2017. doi:10.1016/j.proci.2016.06.047.

[16] R. Demarco, F. Nmira, and J. L. Consalvi. Influence of thermal radiation on soot production in Laminar axisymmetric diffusion flames. *Journal of Quantitative Spectroscopy and Radiative Transfer*, 120:52–69, 2013. doi:10.1016/j.jqsrt.2013.02.004.

[17] R. A. Dobbins and C. M. Megaridis. Morphology of Flame-Generated Soot As Determined by Thermophoretic Sampling. *Langmuir*, 3(2):254–259, 1987. doi:10.1021/la00074a019.

[18] J. A. H. Dreyer, M. Poli, N. Eaves, M. L. Botero, J. Akroyd, S. Mosbach, and M. Kraft. Evolution of the soot particle size distribution along the centreline of a *n* -heptane / toluene co-flow diffusion flame. *Combustion and Flame*, 209(206): 256–266, 2019. doi:10.1016/j.combustflame.2019.08.002.

[19] J. A. H. Dreyer, R. I. Slavchov, E. J. Rees, J. Akroyd, M. Salamanca, S. Mosbach, and M. Kraft. Improved methodology for performing the inverse Abel transform of flame images for color ratio pyrometry. *Applied Optics*, 58(10):2662, 2019. doi:10.1364/AO.58.002662.

[20] D. Duca, C. Irimiea, A. Faccinetto, J. A. Noble, M. Vojkovic, Y. Carpentier, I. K. Ortega, C. Pirim, and C. Focsa. On the benefits of using multivariate analysis in mass spectrometric studies of combustion-generated aerosols. *Faraday Discussions*, 218:115–137, 2019. doi:10.1039/c8fd00238j.

[21] A. C. Ferrari. Raman spectroscopy of graphene and graphite: Disorder, electron-phonon coupling, doping and nonadiabatic effects. *Solid State Communications*, 143(1-2):47–57, 2007. doi:10.1016/j.ssc.2007.03.052.

[22] A. C. Ferrari and D. M. Basko. Raman spectroscopy as a versatile tool for studying the properties of graphene. *Nature nanotechnology*, 8(4):235–46, 2013. doi:10.1038/nnano.2013.46.

[23] A. C. Ferrari and J. Robertson. Interpretation of Raman spectra of disordered and amorphous carbon. *Physical Review B*, 61(20):14 295, 2000. doi:10.1103/PhysRevB.61.14095.

[24] M. Frenklach. Reaction mechanism of soot formation in flames. *Physical Chemistry Chemical Physics*, 4(11):2028–2037, 2002. doi:10.1039/b110045a.

[25] M. Frenklach, R. I. Singh, and A. M. Mebel. On the low-temperature limit of HACA. *Proceedings of the Combustion Institute*, 37(1):969–976, 2019. doi:10.1016/j.proci.2018.05.068.

[26] J. Gau, D. Das, C. S. McEnally, D. Giassi, N. Kempema, and M. B. Long. Yale Coflow Diffusion Flames, 2014. URL `http://guilford.eng.yale.edu/yalecoflowflames/burners.html`.

[27] I. Glassman. Soot formation in combustion processess. *Proceedings of the Combustion Institute*, 22(1):295–311, 1989. doi:10.1016/S0082-0784(89)80036-0.

[28] I. Glassman and P. Yaccarino. The temperature effect in sooting diffusion flames. *Symposium (International) on Combustion*, 18(1):1175–1183, 1981. doi:10.1016/S0082-0784(81)80122-1.

[29] W. J. Grieco, J. B. Howard, L. C. Rainey, and J. B. Vander Sande. Fullerenic carbon in combustion-generated soot. *Carbon*, 38(4):597–614, 2000. doi:10.1016/S0008-6223(99)00149-9.

[30] N. Hansen, M. Schenk, K. Moshammer, and K. Kohse-Höinghaus. Investigating repetitive reaction pathways for the formation of polycyclic aromatic hydrocarbons in combustion processes. *Combustion and Flame*, 180:250–261, 2017. doi:10.1016/j.combustflame.2016.09.013.

[31] K. Hayashida, T. Mogi, K. Amagai, and M. Arai. Growth characteristics of polycyclic aromatic hydrocarbons in dimethyl ether diffusion flame. *Fuel*, 90(2):493–498, 2011. doi:10.1016/j.fuel.2010.10.012.

[32] K. Hayashida, S. Nagaoka, and H. Ishitani. Growth and oxidation of graphitic crystallites in soot particles within a laminar diffusion flame. *Fuel*, 128:148–154, 2014. doi:10.1016/j.fuel.2014.03.008.

[33] H. Hepp and K. Siegmann. Mapping of soot particles in a weakly sooting diffusion flame by aerosol techniques. *Combustion and Flame*, 115(1-2):275–283, 1998. doi:10.1016/S0010-2180(97)00346-5.

[34] O. Herbinet, A. Rodriguez, B. Husson, F. Battin-Leclerc, Z. Wang, Z. Cheng, and F. Qi. Study of the Formation of the First Aromatic Rings in the Pyrolysis of Cyclopentene. *Journal of Physical Chemistry A*, 120(5):668–682, 2016. doi:10.1021/acs.jpca.5b09203.

[35] K. H. Homann. Fullerenes and soot formation - new pathways to large particles in flames. *Angewandte Chemie - International Edition*, 37(18): 2434–2451, 1998. doi:10.1002/(SICI)1521-3773(19981002)37:18<2434::AID-ANIE2434>3.0.CO;2-L.

[36] C. H. Huang and R. L. Vander Wal. Partial premixing effects upon soot nanostructure. *Combustion and Flame*, 168:403–408, 2016. doi:10.1016/j.combustflame.2016.01.006.

[37] F. Inal and S. M. Senkan. Effects of equivalence ratio on species and soot concentrations in premixed *n*-heptane flames. *Combustion and Flame*, 131(1-2):16–28, 2002. doi:10.1016/S0010-2180(02)00388-7.

[38] C. Irimiea, A. Faccinetto, Y. Carpentier, I. K. Ortega, N. Nuns, E. Therssen, P. Desgroux, and C. Focsa. A comprehensive protocol for chemical analysis of flame combustion emissions by secondary ion mass spectrometry. *Rapid Communications in Mass Spectrometry*, 32(13):1015–1025, 2018. doi:10.1002/rcm.8133.

[39] K. O. Johansson, T. Dillstrom, P. Elvati, M. F. Campbell, P. E. Schrader, D. M. Popolan-Vaida, N. K. Richards-Henderson, K. R. Wilson, A. Violi, and H. A. Michelsen. Radical-radical reactions, pyrene nucleation, and incipient soot formation in combustion. *Proceedings of the Combustion Institute*, 36(1):799–806, 2017. doi:10.1016/j.proci.2016.07.130.

[40] K. O. Johansson, M. P. Head-Gordon, P. E. Schrader, K. R. Wilson, and H. A. Michelsen. Resonance-stabilized hydrocarbon-radical chain reactions may explain soot inception and growth. *Science*, 361(6406):997–1000, 2018. doi:10.1126/science.aat3417.

[41] A. E. Karataş, G. Intasopa, and Ö. L. Gülder. Sooting behaviour of *n*-heptane laminar diffusion flames at high pressures. *Combustion and Flame*, 160(9):1650–1656, 2013. doi:10.1016/j.combustflame.2013.03.008.

[42] I. M. Kennedy, C. Yam, D. C. Rapp, and R. J. Santoro. Modeling and measurements of soot and species in a laminar diffusion flame. *Combustion and Flame*, 107(4): 368–382, 1996. doi:10.1016/S0010-2180(96)00092-2.

[43] M. R. Kholghy, Y. Afarin, A. D. Sediako, J. Barba, M. Lapuerta, C. Chu, J. Weingarten, B. Borshanpour, V. Chernov, and M. J. Thomson. Comparison of multiple diagnostic techniques to study soot formation and morphology in a diffusion flame. *Combustion and Flame*, 176:567–583, 2017. doi:10.1016/j.combustflame.2016.11.012.

[44] Z. Klimont, K. Kupiainen, C. Heyes, P. Purohit, J. Cofala, P. Rafaj, J. Borken-Kleefeld, and W. Schöpp. Global anthropogenic emissions of particulate matter including black carbon. *Atmospheric Chemistry and Physics*, 17(14):8681–8723, 2017. doi:10.5194/acp-17-8681-2017.

[45] D. S. Knight and W. B. White. Characterization of diamond films by Raman spectroscopy. *Journal of Materials Research*, 4(2):385–393, 1989. doi:10.1557/jmr.1989.0385.

[46] H. W. Kroto and K. McKay. The formation of quasi-icosahedral spiral shell carbon particles. *Nature*, 331:328–331, 1988. doi:10.1038/331328a0.

[47] A. L. Lafleur, J. B. Howard, J. A. Marr, and T. Yadav. Proposed fullerene precursor corannulene identified in flames both in the presence and absence of fullerene production. *Journal of physical chemistry*, 97(51):13539–13543, 1993. doi:10.1021/j100153a020.

[48] A. Lamprecht, B. Atakan, and K. Kohse-Höinghaus. Fuel-rich flame chemistry in low-pressure cyclopentene flames. *Proceedings of the Combustion Institute*, 28(2): 1817–1824, 2000. doi:10.1016/s0082-0784(00)80584-6.

[49] P. J. Landrigan, R. Fuller, N. J. R. Acosta, O. Adeyi, R. Arnold, N. N. Basu, A. B. Baldé, R. Bertollini, S. Bose-O'Reilly, J. I. Boufford, P. N. Breysse, T. Chiles, C. Mahidol, A. M. Coll-Seck, M. L. Cropper, J. Fobil, V. Fuster, M. Greenstone, A. Haines, D. Hanrahan, D. Hunter, M. Khare, A. Krupnick, B. Lanphear, B. Lohani, K. Martin, K. V. Mathiasen, M. A. McTeer, C. J. L. Murray, J. D. Ndahimananjara, F. Perera, J. Potočnik, A. S. Preker, J. Ramesh, J. Rockström, C. Salinas, L. D. Samson, K. Sandilya, P. D. Sly, K. R. Smith, A. Steiner, R. B. Stewart, W. A. Suk, O. C. P. van Schayck, G. N. Yadama, K. Yumkella, and M. Zhong. The Lancet Commission on pollution and health. *Lancet (London, England)*, 391(10119):462–512, 2018. doi:10.1016/S0140-6736(17)32345-0.

[50] R. P. Lindstedt and L. Q. Maurice. Detailed Kinetic Modelling of *n*-heptane Combustion. *Combustion Science and Technology*, 107(4-6):317–353, 1995. doi:10.1080/00102209508907810.

[51] F. Liu, H. Guo, G. J. Smallwood, and Ö. L. Gülder. Effects of gas and soot radiation on soot formation in a coflow laminar ethylene diffusion flame. *Journal of Quantitative Spectroscopy and Radiative Transfer*, 73(2-5):409–421, 2002. doi:10.1016/S0022-4073(01)00205-9.

[52] P. M. Mandatori and Ö. L. Gülder. Soot formation in laminar ethane diffusion flames at pressures from 0.2 to 3.3 MPa. *Proceedings of the Combustion Institute*, 33(1): 577–584, 2011. doi:10.1016/j.proci.2010.06.004.

[53] J. W. Martin, R. I. Slavchov, E. K. Yapp, J. Akroyd, S. Mosbach, and M. Kraft. The Polarization of Polycyclic Aromatic Hydrocarbons Curved by Pentagon Incorporation: The Role of the Flexoelectric Dipole. *Journal of Physical Chemistry C*, 121 (48):27154–27163, 2017. doi:10.1021/acs.jpcc.7b09044.

[54] J. W. Martin, M. Botero, R. I. Slavchov, K. Bowal, J. Akroyd, S. Mosbach, and M. Kraft. Flexoelectricity and the Formation of Carbon Nanoparticles in Flames. *Journal of Physical Chemistry C*, 122(38):22210–22215, 2018. doi:10.1021/acs.jpcc.8b08264.

[55] J. W. Martin, D. Hou, A. Menon, J. Akroyd, X. You, and M. Kraft. Reactivity of Polycyclic Aromatic Hydrocarbon Soot Precursors: Implications of Localised π-Radicals on Rim-based Pentagonal Rings. *The Journal of Physical Chemistry C*, 123:26673–26682, 2019. doi:10.1021/acs.jpcc.9b07558.

[56] J. W. Martin, A. Menon, C. T. Lao, J. Akroyd, and M. Kraft. Dynamic polarity of curved aromatic soot precursors. *Combustion and Flame*, 206:150–157, 2019. doi:10.1016/j.combustflame.2019.04.046.

[57] C. McEnally, D. D. Das, and L. D. Pfefferle. Yield Sooting Index Database Volume 2: Sooting Tendencies of a Wide Range of Fuel Compounds on a Unified Scale. Technical report, Yale University, 2017. URL https://dataverse.harvard.edu/dataset.xhtml;jsessionid=b8c78cd0705e41a43cdfedf496f9?persistentId=doi:10.7910/DVN/7HGFT8.

[58] C. S. McEnally and L. D. Pfefferle. The Effects of Slight Premixing on Fuel Decomposition and Hydrocarbon Growth in Benzene-Doped Methane Nonpremixed Flames. *Combustion and Flame*, 129(3):305–323, 2002. doi:https://doi.org/10.1016/S0010-2180(02)00347-4.

[59] C. S. McEnally and L. D. Pfefferle. Experimental study of fuel decomposition and hydrocarbon growth processes for cyclohexane and related compounds in nonpremixed flames. *Combustion and Flame*, 136(1-2):155–167, 2004. doi:10.1016/j.combustflame.2003.09.012.

[60] C. S. McEnally and L. D. Pfefferle. Fuel decomposition and hydrocarbon growth processes for substituted cyclohexanes and for alkenes in nonpremixed flames. *Proceedings of the Combustion Institute*, 30(1):1425–1432, 2005. doi:10.1016/j.proci.2004.08.048.

[61] C. S. McEnally, Ü. Ö. Köylü, L. D. Pfefferle, and D. E. Rosner. Soot volume fraction and temperature measurements in laminar nonpremixed flames using thermocouples. *Combustion and Flame*, 2180(97):701–720, 1997. doi:10.1016/S0010-2180(97)00054-0.

[62] C. S. McEnally, A. M. Schaffer, M. Long, L. Pfefferle, M. D. Smooke, M. B. Colket, and R. J. Hall. Computational and experimental study of soot formation in a coflow, laminar diffusion flame. *Proceedings of the Combustion Institute*, 117(1):1497–1505, 1998. doi:10.1016/S0010-2180(98)00096-0.

[63] C. S. McEnally, D. M. Ciuparu, and L. D. Pfefferle. Experimental study of fuel decomposition and hydrocarbon growth processes for practical fuel components: heptanes. *Combustion and Flame*, 134(4):339–353, 2003. doi:10.1016/S0010-2180(03)00113-5.

[64] C. S. McEnally, L. D. Pfefferle, B. Atakan, and K. Kohse-Höinghaus. Studies of aromatic hydrocarbon formation mechanisms in flames: Progress towards closing the fuel gap. *Progress in Energy and Combustion Science*, 32(3):247–294, 2006. doi:10.1016/j.pecs.2005.11.003.

[65] C. F. Melius, M. E. Colvin, N. M. Marinov, W. J. Pitz, and S. M. Senkan. Reaction mechanisms in aromatic hydrocarbon formation involving the C5H5 cyclopentadienyl moiety. *Symposium (International) on Combustion*, 26(1):685–692, 1996. doi:10.1016/s0082-0784(96)80276-1.

[66] X. Mercier, O. Carrivain, C. Irimiea, A. Faccinetto, and E. Therssen. Dimers of polycyclic aromatic hydrocarbons: The missing pieces in the soot formation process. *Physical Chemistry Chemical Physics*, 21(16):8285–8294, 2019. doi:10.1039/c9cp00394k.

[67] H. A. Michelsen. Probing soot formation, chemical and physical evolution, and oxidation: A review of in situ diagnostic techniques and needs. *Proceedings of the Combustion Institute*, 36(1):717–735, 2017. doi:10.1016/j.proci.2016.08.027.

[68] A. Mukherjee and M. Agrawal. World air particulate matter: sources, distribution and health effects. *Environmental Chemistry Letters*, 15(2):283–309, 2017. doi:10.1007/s10311-017-0611-9.

[69] T. U. of Adelaide Centre for Energy Technology. International Sooting Flame (ISF) workshop, 2019. URL `https://www.adelaide.edu.au/cet/isfworkshop/`.

[70] B. Öktem, M. P. Tolocka, B. Zhao, H. Wang, and M. V. Johnston. Chemical species associated with the early stage of soot growth in a laminar premixed ethylene-oxygen-argon flame. *Combustion and Flame*, 142(4):364–373, 2005. doi:10.1016/j.combustflame.2005.03.016.

[71] S. A. Pfau, A. La Rocca, and M. W. Fay. Quantifying soot nanostructures: Importance of image processing parameters for lattice fringe analysis. *Combustion and Flame*, 211:430–444, 2020. doi:10.1016/j.combustflame.2019.10.020.

[72] C. J. Pope, J. A. Marr, and J. B. Howard. Chemistry of fullerenes C60 and C70 formation in flames. *Journal of Physical Chemistry*, 97(42):11001–11013, 1993. doi:10.1021/j100144a018.

[73] A. Raj. Structural effects on the growth of large polycyclic aromatic hydrocarbons by C_2H_2. *Combustion and Flame*, 204:331–340, 2019. doi:10.1016/j.combustflame.2019.03.027.

[74] A. Raj, S. Y. Yang, D. Cha, R. Tayouo, and S. H. Chung. Structural effects on the oxidation of soot particles by O_2: Experimental and theoretical study. *Combustion and Flame*, 160(9):1812–1826, 2013. doi:10.1016/j.combustflame.2013.03.010.

[75] H. Richter and J. Howard. Formation of polycyclic aromatic hydrocarbons and their growth to soot – a review of chemical reaction pathways. *Progress in Energy and Combustion Science*, 26(4-6):565–608, 2000. doi:10.1016/S0360-1285(00)00009-5.

[76] C. Russo, A. Tregrossi, and A. Ciajolo. Dehydrogenation and growth of soot in premixed flames. *Proceedings of the Combustion Institute*, 35(2):1803–1809, 2015. doi:10.1016/j.proci.2014.05.024.

[77] L. G. Scanlon, P. B. Balbuena, Y. Zhang, G. Sandi, C. K. Back, W. A. Feld, J. Mack, M. A. Rottmayer, and J. L. Riepenhoff. Investigation of Corannulene for Molecular Hydrogen Storage via Computational Chemistry and Experimentation. *The Journal of Physical Chemistry B*, 110(15):7688–7694, 2006. doi:10.1021/jp0574403.

[78] F. Schulz, M. Commodo, K. Kaiser, G. De Falco, P. Minutolo, G. Meyer, A. D'Anna, and L. Gross. Insights into incipient soot formation by atomic force microscopy. *Proceedings of the Combustion Institute*, 37(1):885–892, 2019. doi:10.1016/j.proci.2018.06.100.

[79] L. Seidel, K. Moshammer, X. Wang, T. Zeuch, K. Kohse-Höinghaus, and F. Mauss. Comprehensive kinetic modeling and experimental study of a fuel-rich, premixed *n*-heptane flame. *Combustion and Flame*, 162(5):2045–2058, 2015. doi:10.1016/j.combustflame.2015.01.002.

[80] S. R. Smith and A. S. Gordon. A Study of the Pyrolysis of Cyclohexene. *The Journal of Physical Chemistry*, 65(7):1124–1128, 1961. doi:10.1021/j100825a008.

[81] M. D. Smooke, R. J. Hall, M. B. Colket, J. Fielding, M. B. Long, C. S. McEnally, and L. D. Pfefferle. Investigation of the transition from lightly sooting towards heavily sooting co-flow ethylene diffusion flames. *Combustion Theory and Modelling*, 8(3): 593–606, 2004. doi:10.1088/1364-7830/8/3/009.

[82] F. Tuinstra and J. L. Koenig. Raman Spectrum of Graphite. *The Journal of Chemical Physics*, 53(3):1126–1130, 1970. doi:10.1063/1.1674108.

[83] M. Uchiyama, T. Tomioka, and A. Amano. Thermal decomposition of cyclohexene. *Journal of Physical Chemistry*, 68(7):1878–1881, 1964. doi:10.1021/j100789a036.

[84] R. L. Vander Wal and A. J. Tomasek. Soot nanostructure: Dependence upon synthesis conditions. *Combustion and Flame*, 136(1-2):129–140, 2004. doi:10.1016/j.combustflame.2003.09.008.

[85] A. Violi. Cyclodehydrogenation reactions to cyclopentafused polycyclic aromatic hydrocarbons. *Journal of Physical Chemistry A*, 109(34):7781–7787, 2005. doi:10.1021/jp052384r.

[86] C. Wang, T. Huddle, C. H. Huang, W. Zhu, R. L. Vander Wal, E. H. Lester, and J. P. Mathews. Improved quantification of curvature in high-resolution transmission electron microscopy lattice fringe micrographs of soots. *Carbon*, 117:174–181, 2017. doi:10.1016/j.carbon.2017.02.059.

[87] H. Wang. Formation of nascent soot and other condensed-phase materials in flames. *Proceedings of the Combustion Institute*, 33(1):41–67, 2011. doi:10.1016/j.proci.2010.09.009.

[88] H. Wang and M. Frenklach. A detailed kinetic modeling study of aromatics formation in laminar premixed acetylene and ethylene flames. *Combustion and Flame*, 110(1-2):173–221, 1997. doi:10.1016/S0010-2180(97)00068-0.

[89] J. Wang, W. Sun, G. Wang, X. Fan, Y.-Y. Lee, C. K. Law, F. Qi, and B. Yang. Understanding benzene formation pathways in pyrolysis of two C6H10 isomers: Cyclohexene and 1,5-hexadiene. *Proceedings of the Combustion Institute*, 37(1): 1091–1098, 2019. doi:10.1016/j.proci.2018.05.051.

[90] Y. Wang, A. Raj, and S. H. Chung. A PAH growth mechanism and synergistic effect on PAH formation in counterflow diffusion flames. *Combustion and Flame*, 160(9): 1667–1676, 2013. doi:10.1016/j.combustflame.2013.03.013.

[91] Y. Wang, A. Makwana, S. Iyer, M. Linevsky, R. J. Santoro, T. A. Litzinger, and J. O'Connor. Effect of fuel composition on soot and aromatic species distributions in laminar, co-flow flames. Part 1. Non-premixed fuel. *Combustion and Flame*, 189: 443–455, 2018. doi:10.1016/j.combustflame.2017.08.011.

[92] Z. Wang, L. Ye, W. Yuan, L. Zhang, Y. Wang, Z. Cheng, F. Zhang, and F. Qi. Experimental and kinetic modeling study on methylcyclohexane pyrolysis and combustion. *Combustion and Flame*, 161(1):84–100, 2014. doi:10.1016/j.combustflame.2013.08.011.

[93] R. Whitesides, A. C. Kollias, D. Domin, W. A. Lester, and M. Frenklach. Graphene layer growth: Collision of migrating five-member rings. *Proceedings of the Combustion Institute*, 31 I(1):539–546, 2007. doi:10.1016/j.proci.2006.07.034.

[94] X. Z. Wu, Y. R. Yao, M. M. Chen, H. R. Tian, J. Xiao, Y. Y. Xu, M. S. Lin, L. Abella, C. B. Tian, C. L. Gao, Q. Zhang, S. Y. Xie, R. B. Huang, and L. S. Zheng. Formation of Curvature Subunit of Carbon in Combustion. *Journal of the American Chemical Society*, 138(30):9629–9633, 2016. doi:10.1021/jacs.6b04898.

[95] K. Yehliu, R. L. Vander Wal, and A. L. Boehman. A comparison of soot nano-structure obtained using two high resolution transmission electron microscopy image analysis algorithms. *Carbon*, 49(13):4256–4268, 2011. doi:10.1016/j.carbon.2011.06.003.

[96] X. You, R. Whitesides, D. Zubarev, W. A. Lester, and M. Frenklach. Bay-capping reactions: Kinetics and influence on graphene-edge growth. *Proceedings of the Combustion Institute*, 33(1):685–692, 2011. doi:10.1016/j.proci.2010.05.110.

[97] T. Yuan, L. Zhang, Z. Zhou, M. Xie, L. Ye, and F. Qi. Pyrolysis of *n*-heptane: Experimental and theoretical study. *Journal of Physical Chemistry A*, 115(9):1593–1601, 2011. doi:10.1021/jp109640z.

[98] A. V. Zabula, A. S. Filatov, S. N. Spisak, A. Y. Rogachev, and M. A. Petrukhina. A main group metal sandwich: five lithium cations jammed between two corannulene tetraanion decks. *Science*, 333(6045):1008–1011, 2011. doi:10.1126/science.1208686.